International Journal of Solids and Structures 243 (2022) 111545

Contents lists available at ScienceDirect

International Journal of Solids and Structures

journal homepage: www.elsevier.com/locate/ijsolstr

A complex-variable finite element method-based inverse methodology to extract constitutive parameters using experimental data

Daniel Ramirez-Tamayo [a,*], Ayoub Soulami [a], Varun Gupta [a,1], David Restrepo [b], Arturo Montoya [b,c], Ethan Nickerson [a], Timothy Roosendaal [a], Kevin Simmons [a], Gayaneh Petrossian [a], Harry Millwater [b]

[a] Pacific Northwest National Labs, Richland, WA, USA
[b] Department of Mechanical Engineering, The University of Texas at San Antonio, San Antonio, TX, USA
[c] Department of Civil and Environmental Engineering, The University of Texas at San Antonio, San Antonio, TX, USA

ARTICLE INFO

Keywords:
Complex-variable finite element method
Inverse methods
Abaqus
UEL
Automatic differentiation

ABSTRACT

This paper presents the use of full-field kinematic measurements obtained using the digital image correlation (DIC) procedure and load–displacement data to determine constitutive material properties by solving an inverse finite element optimization problem. A key ingredient in the proposed approach is computing accurate sensitivities with respect to the unknown parameters. These sensitivities were used to solve the optimization problem using an accurate, efficient, gradient-based method, and were computed using the complex-variable finite element method, ZFEM. The use of ZFEM's gradients to inversely determine material properties is demonstrated with two examples. First, the elastic–plastic material properties of DP-590 steel are obtained using a tensile test specimen. Second, the cohesive material parameters of an adhesive are determined using a double cantilever beam test. A significant outcome of this paper is that the use of a weighted residual formulation of the interfacial strain fields and the load–displacement data within the optimization procedure provides better estimates of the constitutive properties than using only the load–displacement data. This technique minimizes the relative error in both the strain fields and the load–displacement curve, which is important to obtain accurate interfacial properties.

1. Introduction

The use of adhesively bonded joints in the automotive and aerospace industries is continuously increasing because they reduce both stress concentrations and weight compared to traditional joining techniques such as welded, bolted, and riveted joint (Ebnesajjad and Landrock, 2014; Ramalho et al., 2020). In addition, adhesively bonded joints allow the effective assembly of multiple lightweight materials such as carbon fiber reinforced composites, aluminum alloys, and high-strength steels, which reduces the structure's weight without compromising its structural performance and increases fuel efficiency. Thus, several analytical, experimental, and numerical methods have been developed to characterize these joints.

The simplest approach among analytical methods is to consider a single-lap joint (SLJ) where the adhesive is considered to deform only in shear. This allows one to obtain an analytical expression for the adhesive shear stress. Using this assumption, (Volkersen, 1938) introduced the concept of differential shear that accounts for the deformation in tension from the adherends. Then, Goland and Reissner (2021) considered the effects of the eccentric load path of an SLJ by adding a bending moment factor and a transverse force factor. These analytical methods have since been replaced by numerical methods, but they provide an indication of the overall strength of the joint. These methods are restricted to very simple geometries and loading cases (Ramalho et al., 2020).

Experimental methods are used to determine the critical energy release rate of a joint, G_c, which quantifies the resistance to crack propagation of an adhesive joint. However, G_c cannot be considered the only property that characterizes the interfacial behavior of a joint because it depends on the mode of loading (modes I, II, and III) (da Silva et al., 2009; Ramirez Tamayo et al., 2018). Hence, different

* Corresponding author.
E-mail addresses: daniel.ramireztamayo@pnnl.gov (D. Ramirez-Tamayo), ayoub.soulami@pnnl.gov (A. Soulami), varun.gupta@exxonmobil.com (V. Gupta), david.restrepo@utsa.edu (D. Restrepo), arturo.montoya@utsa.edu (A. Montoya), ethan.nickerson@pnnl.gov (E. Nickerson), timothy.roosendaal@pnnl.gov (T. Roosendaal), kl.simmons@pnnl.gov (K. Simmons), gayaneh.petrossian@pnnl.gov (G. Petrossian), harry.millwater@utsa.edu (H. Millwater).
[1] Currently at ExxonMobil Upstream Research Company; work was performed while still at PNNL.

https://doi.org/10.1016/j.ijsolstr.2022.111545
Received 29 September 2021; Received in revised form 23 November 2021; Accepted 28 February 2022
Available online 8 March 2022

tests are used to characterize the critical energy release rate for each mode of loading of an adhesive joint. The most commonly used tests to obtain the mode-I critical energy release rate (G_{Ic}) are the double cantilever beam (DCB) (Prasad and Carlsson, 1994), the tapered double cantilever beam (TDCB) (Marzi et al., 2011) and the single-edge notched bending (SENB) tests (Quan et al., 2018). Similarly, to obtain the mode-II critical energy release rate (G_{IIc}), one can use the end-notched flexure (ENF) test (Ji et al., 2012), or the four-point ENF (4ENF) test (Wang et al., 2009). For problems dealing with mode mixity, Reeder and Crews (Reeder and Crews, 1990) determined G_c for a wide range of mixed-mode ratios for a mixed-mode bending specimen by combining the DCB and the ENF tests on a laminated composite. However, all previous experimental techniques to characterize adhesive joints place restrictions on the test geometries and require the existence of analytical solutions (Shah et al., 1995; van Mier and van Vliet, 2002).

The cohesive zone model (CZM), a numerical technique presented by Barenblatt (Barenblatt, 1959) and Dugdale (Dugdale, 1960), has been widely used to investigate fracture, seams, and joints (Mi et al., 1998). In the CZM formulation, the traction values at the interface and the separation of the adherend surfaces are related through a constitutive law. For mode-I (normal) loading, the traction–displacement behavior of the adhesive joint is governed by two parameters: the mode-I fracture toughness, ϕ_N, and the normal cohesive strength, σ_{max}. Typically, the CZM parameters (ϕ_N and σ_{max}) are determined by matching a numerical simulation to the experimental-load displacement curve (Valoroso et al., 2013). However, this approach might result in inaccuracies on the adopted model because the solution is not unique and several combinations of the cohesive parameters can re-create the global behavior (load–displacement) of the joint, while the near interface strain fields are incorrect (Shen and Paulino, 2011; Ramirez-Tamayo et al., 2021; Liljedahl et al., 2006). In addition, the existing mechanical test techniques to obtain the CZM parameters place restrictions on the test geometries and sometimes require the existence of analytical solutions, making these techniques unsuitable for joints obtained using new technologies such as Friction stir Assisted Scribe Technique (FAST) (Wang et al., 2020). To address this issue, some inverse methods use full-field kinematic data obtained using the digital image correlation (DIC) method, and obtain the cohesive parameters by solving an optimization problem by minimizing the discrepancy between simulated and experimental results. Shen and Paulino (Shen and Paulino, 2011) used DIC data from SENB specimens to inversely determine the elastic properties of bulk materials through a gradient-free minimization process. Then, using the same approach, they determined the cohesive fracture properties of the adhesive. The use of a gradient-free method adds simplicity because derivatives are usually difficult to obtain during finite element (FE) analysis. However, gradient-free methods are known to converge more slowly than gradient-based methods (Ramirez-Tamayo et al., 2021).

The hypercomplex-variable FE method, ZFEM, incorporates the complex Taylor series expansion (CTSE) method (Squire and Trapp, 1998) to compute highly accurate, subtraction-error-free derivatives within an FE analysis. Through a systematic complexification of an existing FE formulation, ZFEM has shown to be an effective tool to compute highly accurate estimates of arbitrary shape, material property, or loading sensitivities. ZFEM has been verified in several engineering areas, such as linear elastic fracture mechanics (Millwater et al., 2016; Aguirre-Mesa et al., 2019), elastic–plastic fracture mechanics (Montoya et al., 2018), thermoelastic fracture (Ramirez-Tamayo et al., 2018), mixed-mode loading and interface cracks (Ramirez Tamayo et al., 2018), and functionally graded materials (Ramirez-Tamayo et al., 2020), among others. All of these applications have been implemented through user element subroutines in Abaqus (2015).

In a recent publication, Ramirez-Tamayo et al. (2021) showed the development of a complex-variable version of the Park–Paulino–Roesler (PPR) cohesive zone element (Park et al., 2009), aka "ZPPR", and its application to determining material properties of an adhesively bonded DCB using synthetically generated experimental data. The ZPPR formulation was shown to compute highly accurate and subtraction-error-free derivatives of the nodal displacements with respect to the unknown cohesive parameters. During optimization, the use of these derivatives resulted in faster convergence and a more accurate answer than either gradient-free or finite-difference gradient methods (Ramirez-Tamayo et al., 2021).

This paper develops a comprehensive optimization algorithm that incorporates DIC-based strain data along with the force–displacement data within a weighted residual formulation. Accurate derivatives computed using ZFEM were used to inversely determine material parameters for two examples. First, the mechanical properties of DP-590 steel were obtained using a tensile test specimen. Second, the cohesive material parameters of an adhesive were determined using a DCB test. The results demonstrate the value of using highly accurate and truncation-error-free first-order derivatives and the advantages of a weighted residual formulation that incorporates DIC strain data.

The paper is organized as follows. First, the methodologies of DIC, cohesive zone modeling, and CTSE are discussed. Then, the Abaqus implementation of the ZFEM is presented. Next, the optimization algorithm is discussed, in which the objective function minimizes the discrepancies between experimental and computational results. Then, two numerical examples are provided that demonstrate use of ZFEM's sensitivities to inversely determine constitutive material parameters for both elastic–plastic and cohesive zone models. Next, a study of the effect of the residual weights on both the load–displacement curve and strain field is presented. Finally, concluding remarks are provided.

2. Background and methodology

2.1. Digital image correlation (DIC)

2.1.1. Overview of the DIC method

DIC is an optical measurement technique that provides full-field deformation measurements of the surface of a sample. A computer program compares images of a sample before and after deformation. The image from before deformation is referred to as the "reference image". The deformation measurements can then be used to determine the in-plane strain over the surface of the sample and, if multiple cameras are used, the out-of-plane deformation as well. To perform a DIC analysis, a high-contrast speckle pattern must first be applied to the surface of the sample to track the deformation over a sequence of images taken during the mechanical testing. The best results are achieved with a pattern that is both isotropic and non-repeating; see Fig. 1. In this work, spray paint along with a stamp and ink were used to apply the pattern.

Deformation is then calculated. First, the reference image is broken into subsets of pixels. For this experiment, the subset used was 25 by 27 pixels. The center-to-center spacing between subsets is called the step size. In this work, the step sizes varied from 7 to 9 pixels. The standard practice is to use a step size that is less than half the size of the subset so that all the available pixels are being used. Each subsequent image is then searched for the same collection of subsets. Once a subset has been found, the displacement vector between the reference and the deformed subsets is calculated; see Fig. 1. This results in a displacement measurement for each subset within the region of interest (ROI). Post-processing of the measured displacements then produces a strain measurement for each subset in each subsequent image. In this paper, the Vic-3D software (Correlated Solutions, Inc., 2010) was used to perform the DIC analysis for both the tensile and DCB tests.

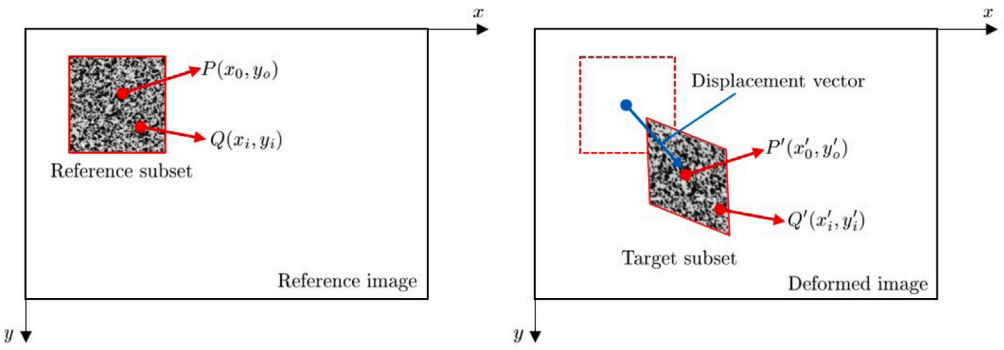

Fig. 1. Speckle pattern and illustration of the undeformed subset and the corresponding deformed subset during a DIC analysis . *Source:* Taken from Pan and Li (2011).

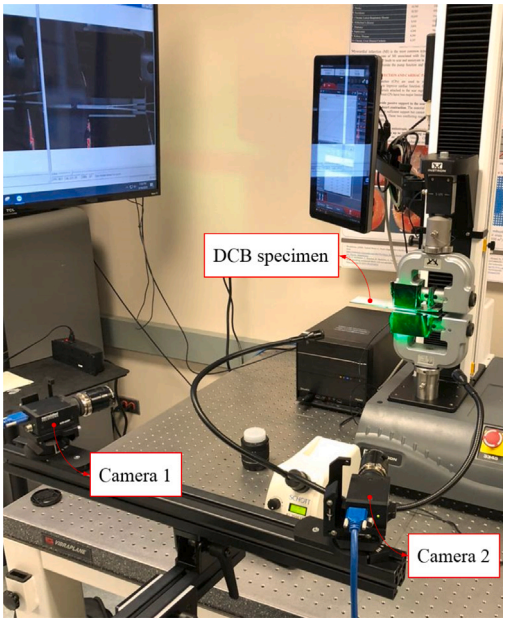

Fig. 2. DIC set-up.

2.1.2. Experimental setup and resulting DIC data (tensile test and DCB)

Tensile tests were performed on DP590 specimens with dimensions according to ASTM standard E8 (ASTM International, 2001). A white base coat was applied using Rust-Oleum 2x spray paint, after which a black speckle pattern was applied using a stamp with an average speckle size of 3 pixels. Two cameras were mounted to a fixture on a tripod and a blue LED light panel provided additional light. Tensile tests were performed using an MTS 312.21 hydraulic testing system. Analog data from this frame was passed to the computer controlling the cameras, which allowed load measurements to be synchronized with images when recorded for each set of pictures, see Fig. 2.

DCB tests were performed using DP590 steel specimens bonded with adhesive (Whitney et al., 1982). Both the white base coat and black speckle pattern were applied using Rust-Oleum 2x cover paint. An ADMET micro tensile frame was used to perform the DCB tests. This frame applied load by moving both the top and bottom grips at the same rate in opposite directions. The symmetric motion was helpful, because displacement of only a single grip would result in translation of the sample, which often causes the specimen to move out of the field of view and may introduce noise in the data. Load data from the frame were passed to the computer controlling the cameras, allowing load measurements to be synchronized with images when recorded for each set of pictures. The experimental parameters used for the tensile and DCB tests are swhon in Table 1.

Table 1
Experimental parameters for tensile and DCB tests.

Hardware parameters	Tensile test	DCB test
Camera	5 MP Basler	12 MP Basler
Lens	50 mm	50 mm
Field of view	43 mm	34 mm
Aperture	f/5.6	f/8.0
Image scale	0.0185 mm/px	0.0185 mm/px
Stereo angle	16°	24°
Stand-off distance	363 mm	204 mm
Image acquisition rate	10 Hz	1 Hz
Speckle size	3 px	3 px
Analysis Parameters		
Software	Vic-3D Version 8.4	Vic-3D Version 8.4
Subset size	25 px	27 px
Step size	9 px	7 px
Strain formulation	Engineering	Engineering
Strain window	15 px	15 px
Calibration Parameters		
Focal length	19,750 px	23,355 px
Distance between cameras	102 mm	86.6 mm

2.1.3. Region of interest and comparison of DIC and FE fields

While performing a DIC analysis, an ROI must be selected by the user. Within this region, the full-field kinematic measurements such as displacements and strains will be obtained and then compared against FE fields. This region must be selected carefully and the DIC lenses must be well focused to obtain good quality measurements. Fig. 3 shows a schematic of the location of the ROI (red shaded region) within a DCB specimen.

Fig. 4 shows the strain in the y-direction (ϵ_{yy}) for two different loading magnitudes during a DCB test. Note that the ROI was selected such that the strain fields near the crack tip were included for the duration of the test.

Section 2.4 shows the computation of the residual function, which reflects the mismatch between computational and experimental data. Hence, direct comparison between DIC data and FE strain fields is needed. However, the DIC strain fields do not necessarily match the location of an FE integration point. Thus, DIC data from nearby points was interpolated to approximate the strain value at the exact location of the FE sample point. Fig. 5 depicts how the interpolation between DIC data and FE strain sampling points was conducted. Six elements that lie within the ROI were chosen, as shown in Fig. 5. Strain values for nearby DIC data points were chosen according to their distance from the point that marks the middle of the FE (black triangles in Fig. 5) to estimate the strain at the element's center. This approach allows a direct comparison between DIC and FE strain fields.

The "scipy.interpolate.griddata" function from SciPy (Virtanen et al., 2020) was used to estimate strain from DIC data to the center of the element. Given the fact that the DIC data density is very high, the SciPy

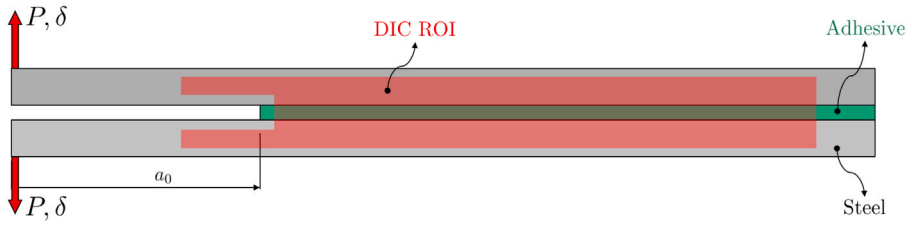

Fig. 3. Location of the ROI within a DCB sample (not to scale).

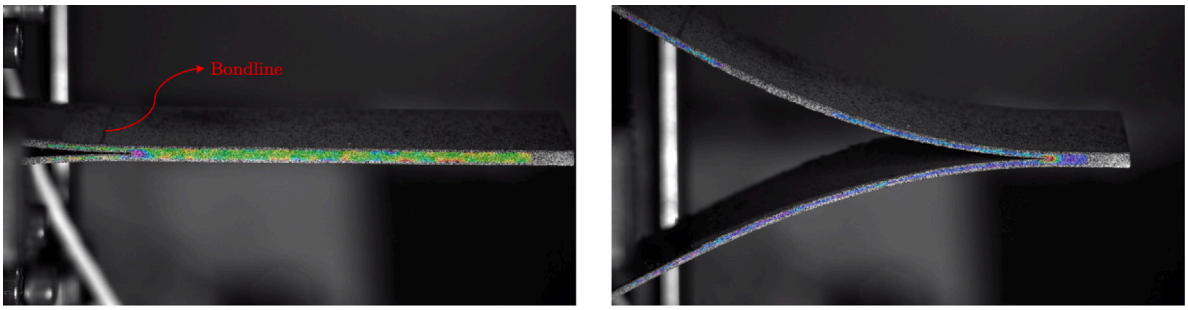

Fig. 4. Strain fields from the ROI during the DIC analysis performed on a DCB sample: (a) Beginning and (b) end of the test.

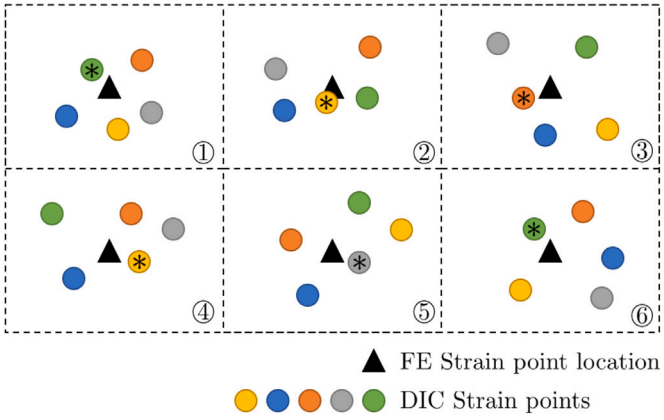

Fig. 5. Schematic of interpolation of DIC data to FE sampling points. The strain value at the nearest DIC point is used at the element Gauss point. An asterisk "*" denotes the DIC data point closest to the FE sampling point.

method "nearest" was used. This algorithm returns the value at the data point closest to the point of interpolation (black triangle/center of the element). For this particular example, element 1 will be assigned the strain value of the green point, element 2 from the yellow, element 3 from the orange, element 4 from yellow, element 5 from gray, and element 6 from green. The DIC point density in the cartoon shown in Fig. 5 was made very low for illustration purposes. For the examples shown in this paper, approximately 40 DIC points lie within each FE.

2.2. Cohesive zone modeling

The CZM has been used to simulate singular crack tip behavior, and thus also can simulate the nonlinear fracture processes of several engineering problems such as adhesively bonded joints (Xu et al., 2003). In the CZM, the stresses ahead of the crack tip are bounded and a traction-separation law is used to describe the fracture process (Freed and Banks-Sills, 2008). Selection of this traction-separation law is a critical aspect of the CZM, because it can lead to a variety of structural responses that in some cases do not reflect experimental observations. These traction-separation relations are either potential-based or non-potential-based. For more information about the available traction-separation laws, refer to Park and Paulino (2013), Park et al. (2016), Ramirez-Tamayo et al. (2021).

In Park and Paulino (2012), Park and Paulino presented a computational implementation of the PPR model (potential-based) (Park et al., 2009), into the commercial FE software Abaqus (Abaqus, 2015), through the use of a user-defined element (UEL) subroutine. The fact that the authors provided source code facilitated the development of a complex-variable version of the PPR cohesive element, aka ZPPR (Ramirez-Tamayo et al., 2021). The ZPPR element enabled the computation of highly accurate first-order derivatives of the nodal displacements and other post-processing quantities such as strain and stresses with respect to all the PPR cohesive parameters. These derivatives were used to inversely determine the interfacial properties of an adhesively bonded DCB with synthetically generated experimental data. It is known that non-potential-based models can provide non-physical behavior for certain separation paths because the model does not always provide a negative tangent stiffness within the softening region (Park et al., 2016). Hence, the ZPPR (potential-based) formulation was selected to re-create the fracture behavior of adhesively bonded joints that will be considered in this paper as well as computing highly accurate first-order derivatives with respect to the cohesive parameters.

The cohesive traction-separation relationship is obtained from the PPR model, in which a fracture potential is given by

$$\Psi(\Delta_n,\Delta_t) = \min(\phi_n,\phi_t) + \left[\Gamma_n\left(1-\frac{\Delta_n}{\delta_n}\right)^{\alpha}\left(\frac{m}{\alpha}+\frac{\Delta_n}{\delta_n}\right)^{m} + \langle\phi_n-\phi_t\rangle\right]\times \left[\Gamma_t\left(1-\frac{|\Delta_t|}{\delta_t}\right)^{\beta}\left(\frac{n}{\beta}+\frac{|\Delta_t|}{\delta_t}\right)^{n} + \langle\phi_t-\phi_n\rangle\right] \quad (1)$$

where Δ is the separation along the fracture surface, Γ is an energy constant, δ is the final crack opening width, α and β are the shape parameters, m and n are dimensionless exponents, and ϕ is the fracture energy. The subscripts "n" and "t" denote normal and tangential directions, respectively, and $\langle.\rangle$ is the Macaulay bracket.

In this cohesive model, four fracture parameters are employed for each fracture mode: fracture energy (ϕ_n and ϕ_t), cohesive strength (σ_{max} and τ_{max}), shape parameters (α and β), and initial slope indicator (λ_n and λ_t). Fig. 6 shows a schematic of the PPR traction-separation

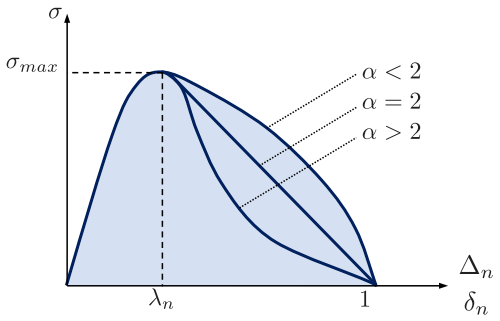

Fig. 6. Potential-based traction-separation law.
Source: Adapted from Park and Paulino (2012).

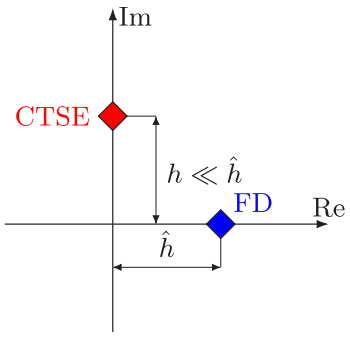

Fig. 7. CTSE vs. FD perturbations.

law for mode-I loading. Softening starts after the normal cohesive strength (σ_{max}) is reached. Complete separation occurs once the final crack opening width (δ_n) is reached, and the area under the ($\sigma_n - \Delta_n$) curve yields the fracture energy (ϕ_n). The normal shape parameter (α) controls the fracture behavior during the softening region. When $\alpha \approx 2$, the PPR model exhibits behavior similar to that of the bilinear model (Wittmann et al., 1988) which is available in most commercial software programs including Abaqus (Abaqus, 2015). More information about potential-based models and the PPR model in particular can be found in Park and Paulino (2012), Park (2009).

2.3. Complex-variable finite element method (ZFEM)

ZFEM calculates sensitivities with respect to variables of interest based on a CTSE method. The CTSE method is a first-order numerical differentiation technique similar in concept but superior to finite differencing (FD). FD requires at least two real-valued-based analyses to obtain the derivative information. In addition, the appropriate step size depends on the problem and its parameters; too large a step size leads to truncation error, while too small a step size leads to subtraction error. In contrast, with CTSE, the derivative information can be obtained in a single FE run and the step size issues associated with FD are circumvented. The perturbation of the variable of interest, x, is made along the imaginary axis, becoming $x^* = x + ih$, where h is the step perturbation size along the imaginary axis and the superscript "*" denotes a complex variable; see Fig. 7. Using the Taylor series, a function f can be expanded as

$$f(x+ih) = f(x) + f^{(1)}(x)\frac{ih}{1!} + f^{(2)}(x)\frac{(ih)^2}{2!} + f^{(3)}(x)\frac{(ih)^3}{3!} + \text{H.O.T.} \quad (2)$$

where H. O. T. denotes higher-order terms, $f^{(1)}$ denotes the first derivative, $f^{(2)}$ the second, etc. Taking the imaginary parts of both sides, Im[ ], solving for the first derivative, and ignoring the $\mathcal{O}(h^2)$ terms, the first derivative can be obtained as

$$f^{(1)}(x) = \frac{df}{dx} \approx \frac{\text{Im}[f(x+ih)]}{h} \quad (3)$$

The step perturbation size h can be made arbitrarily small with no concern about round-off error (Squire and Trapp, 1998). Hence, higher-order effects of $O(h^2)$ can be made negligible through the use of a small h. The Appendix shows the use of the CTSE method to obtain numerically exact derivatives of a multivariate function.

The CTSE method can be implemented within an FE code through a systematic complexification of its formulation. ZFEM has been implemented in Abaqus through a user element subroutine (UEL) (Ramirez Tamayo et al., 2018; Ramirez-Tamayo et al., 2021; Millwater et al., 2016; Aguirre-Mesa et al., 2019; Montoya et al., 2018; Ramirez-Tamayo et al., 2018; Montoya et al., 2015; Gomez-Farias et al., 2015).

2.3.1. ZFEM Abaqus implementation

ZFEM has been implemented in Abaqus through the complexification of a user element subroutine (UEL) (Ramirez Tamayo et al., 2018; Ramirez-Tamayo et al., 2021; Millwater et al., 2016; Aguirre-Mesa et al., 2019; Montoya et al., 2018; Ramirez-Tamayo et al., 2018; Montoya et al., 2015; Gomez-Farias et al., 2015). In a real-valued UEL, the elemental stiffness matrix, $\mathbf{K}_e$, and load vector, $\mathbf{f}_e$, are computed and returned to Abaqus for assembly and solution of the system of equations

$$\mathbf{Ku} = \mathbf{f} \quad (4)$$

where $\mathbf{K}$, $\mathbf{u}$ and $\mathbf{f}$ are the global stiffness matrix, displacement vector, and force vector, respectively.

In ZFEM, the FE variables are now complex and the solution of a complex-valued system of equations is needed. As Abaqus does not have a built-in complex solver, a Cauchy–Riemann (CR) representation of a complex variable must be employed to return a real-valued system of equations to Abaqus. This results in a $2N \times 2N$ system of equations, where N is the number of real degrees of freedom. The additional runtime using ZFEM depends upon the analysis type. For an analysis using the ZPPR element with a symmetric solver, the additional computing time is approximately half that of a real analysis (Ramirez-Tamayo et al., 2021). Eqs. (5) and (6) show the complex system of equations and its CR representation used in a ZFEM analysis:

$$\mathbf{K}^*\mathbf{u}^* = \mathbf{f}^* \quad (5)$$

$$\begin{bmatrix} \mathbf{K}_{\text{Re}} & -\mathbf{K}_{\text{Im}} \\ \mathbf{K}_{\text{Im}} & \mathbf{K}_{\text{Re}} \end{bmatrix} \begin{bmatrix} \mathbf{u}_{\text{Re}} \\ \mathbf{u}_{\text{Im}} \end{bmatrix} = \begin{bmatrix} \mathbf{f}_{\text{Re}} \\ \mathbf{f}_{\text{Im}} \end{bmatrix} \quad (6)$$

where an asterisk * denotes a complex variable and the subscripts "Re" and "Im" denote the real and imaginary components of a complex variable, respectively. After the CR system of equations is solved, the displacement vector contains the nodal displacements and their derivatives with respect to the perturbed variable (PPR variables in this case). Other quantities such as strains, stresses, and potential energy can be computed using the complex nodal displacement vector.

In Ramirez-Tamayo et al. (2021), the authors discussed the steps necessary to complexify an existing Abaqus UEL implementation-in particular, the PPR element (Park and Paulino, 2012). The described process is a generic approach that can be used to obtain highly accurate derivatives. In addition, as demonstrated in Aguirre-Mesa et al. (2019), Ramirez-Tamayo et al. (2020), with the use of a hypercomplex-variable library such as MultiZ (Aguirre-Mesa et al., 2020), higher-order derivatives can be obtained with this approach (Lantoine et al., 2012).

Modifications to the input file and UEL source code are required to compute first-order sensitivities using ZFEM. The nodes must be duplicated in the input file to represent the imaginary nodes and then form a complex-valued element; see Fig. 8. If a displacement boundary

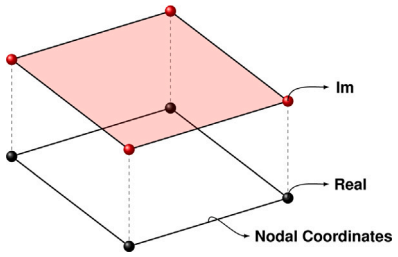

Fig. 8. Eight-noded (four real and four imaginary) element.

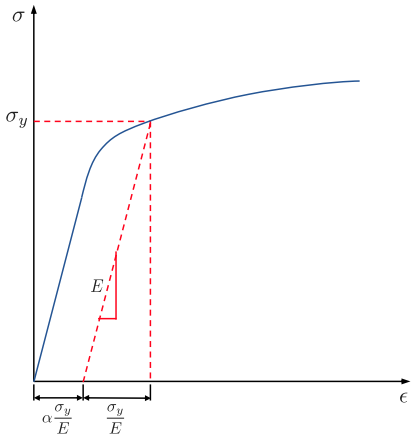

Fig. 9. Stress–strain curve using Ramberg–Osgood material model.

condition is specified in the real-valued analysis, the corresponding imaginary degrees of freedom must also be constrained through the input file.

A few procedures are required in order to implement the complex-variable operations. First, the UEL variables that are affected by the perturbed variable (variable of interest) must be redefined as complex-type. Then, the stiffness matrix and right-hand side vector must be converted to CR form before being returned to Abaqus for assembly and solution of the system of equations. The CR expansion is necessary because Abaqus lacks a complex-type solver. Ramirez-Tamayo et al. (Ramirez-Tamayo et al., 2021) discussed these changes in the context of creating the complex-valued version of the PPR element (ZPPR) and its input file.

2.3.2. Ramberg–Osgood material model

The Ramberg–Osgood material model was used in ZFEM's simulations to describe the nonlinear post-yielding behavior of a material (Ramberg and Osgood, 1943) (Section 3.1). This material model has previously been used with ZFEM for sensitivity analysis and to compute the energy release rate in nonlinear materials undergoing plastic deformation (Montoya et al., 2018, 2015). The one-dimensional model consists of the superposition of a linear elastic term and a power-law term:

$$\epsilon E = \sigma + \alpha \left(\frac{\sigma}{\sigma_y}\right)^{n-1} \sigma \tag{7}$$

where ϵ is the strain, σ is stress, E is the elastic modulus, σ_y is the yield strength, and n and α are material constants describing the hardening behavior of the material. The value $\alpha\sigma_y/E$ is the yield offset, which is equal to 0.2% (see Fig. 9).

Eq. (7) is generalized to multiaxial stress states as

$$\epsilon E = (1+\nu)\mathbf{S} + (1-2\nu)p\mathbf{I} + \frac{3}{2}\alpha \left(\frac{\sigma_e}{\sigma_y}\right)^{n-1} \mathbf{S} \tag{8}$$

where ν is the Poisson's ratio, $\mathbf{S}$ is the stress deviator tensor, p is the hydrostatic stress, and σ_e is the effective von-Mises stress.

2.4. Optimization framework

The mode-I traction-separation behavior of the PPR constitutive model is defined by four parameters: normal fracture energy (ϕ_n), maximum normal traction (σ_{max}), normal shape parameter (α), and the normal slope indicator (λ_n). To inversely determine the cohesive material parameters, a residual function, w, which compares the experimental and computational load–displacement curves and DIC data, is defined as

$$w(\boldsymbol{\theta}) = \alpha_P \left\|\boldsymbol{R}_P\right\|^2 + \alpha_{\epsilon_{yy}} \left\|\boldsymbol{R}_{\epsilon_{yy}}\right\|^2 \tag{9}$$

where $\boldsymbol{\theta}$ is a vector consisting of the material parameters to be optimized as

$$\boldsymbol{\theta} = \begin{bmatrix} \phi_n \\ \sigma_{max} \\ \vdots \\ E \\ \nu \\ \sigma_y \end{bmatrix} \tag{10}$$

and $\boldsymbol{R}_P$ and $\boldsymbol{R}_{\epsilon_{yy}}$ are the residual vectors of the reaction force and the strain in the yy-direction, respectively, computed as

$$\boldsymbol{R}_P = \sum_t \frac{P^{\text{DIC}} - P^{\text{ZFEM}}(\boldsymbol{\theta})}{\|P^{\text{DIC}}\|}; \quad \boldsymbol{R}_{\epsilon_{yy}} = \frac{1}{N_{\epsilon_{points}}} \sum_t \sum_{N_{\epsilon_{points}}} \frac{\epsilon_{yy}^{\text{DIC}} - \epsilon_{yy}^{\text{ZFEM}}(\boldsymbol{\theta})}{\|\epsilon_{yy}^{\text{DIC}}\|}$$

where the superscripts "DIC" and "ZFEM" denote the reaction forces obtained experimentally and computationally, respectively. α_P and $\alpha_{\epsilon_{yy}}$ are the weights of each residual and these weights sum to one. The load residual, $\boldsymbol{R}_P$, is computed for every loading increment, t, of the FE simulation. Similarly, the strain residual, $\boldsymbol{R}_{\epsilon_{yy}}$, is computed for every loading increment (t) and for every point within the ROI ($N_{\epsilon_{points}}$); see Section 2.1.3 for more about the ROI and how the DIC strain field is compared against FE data. This approach can also be used to determine the material properties that govern the mechanical response of a material after certain behavior such as the Ramberg–Osgood material law (see Section 2.3.2).

The optimization procedure is defined as

$$\boldsymbol{\theta} = \arg\min_{\boldsymbol{\theta}} w(\boldsymbol{\theta}) \tag{11}$$

where a gradient-based optimization algorithm will be used for its solution.

For a gradient-based optimization algorithm, the derivatives of the FE output variables with respect to the unknown parameters must be computed. In this section, ZFEM will be used to compute the derivatives of the FE solution vector with respect to the cohesive fracture parameters that govern the interfacial behavior of an adhesively bonded joint; see Section 2.2. Using ZFEM allows one to compute the derivative of the residual function with respect to the cohesive material parameters as

$$\frac{\partial w(\boldsymbol{\theta})}{\partial \theta_i} = 2\alpha_P \left(\frac{P^{\text{DIC}} - P^{\text{ZFEM}}(\boldsymbol{\theta})}{\|P^{\text{DIC}}\|}\right) \frac{\partial \boldsymbol{R}_P}{\partial \theta_i} + 2\alpha_{\epsilon_{yy}} \left(\frac{\epsilon_{yy}^{\text{DIC}} - \epsilon_{yy}^{\text{ZFEM}}(\boldsymbol{\theta})}{\|\epsilon_{yy}^{\text{DIC}}\|}\right) \frac{\partial \boldsymbol{R}_{\epsilon_{yy}}}{\partial \theta_i} \tag{12}$$

where $\theta_i (i = 1, \ldots, N_\theta)$ is the ith element from the solution vector $\boldsymbol{\theta}$ and N_θ is the number of material properties to be optimized. The derivatives of the load and strain residuals, $\boldsymbol{R}_P$ and $\boldsymbol{R}_{\epsilon_{yy}}$, are given by

$$\frac{\partial \boldsymbol{R}_P}{\partial \theta_i} = \sum_t \frac{\frac{-\partial P^{\text{ZFEM}}}{\partial \theta_i}}{\|P^{\text{DIC}}\|}, \quad \frac{\partial \boldsymbol{R}_{\epsilon_{yy}}}{\partial \theta_i} = \frac{1}{N_{\epsilon_{points}}} \sum_t \sum_{\epsilon_{points}} \frac{\frac{-\partial \epsilon_{yy}^{\text{ZFEM}}}{\partial \theta_i}}{\|\epsilon_y^{\text{DIC}}\|} \tag{13}$$

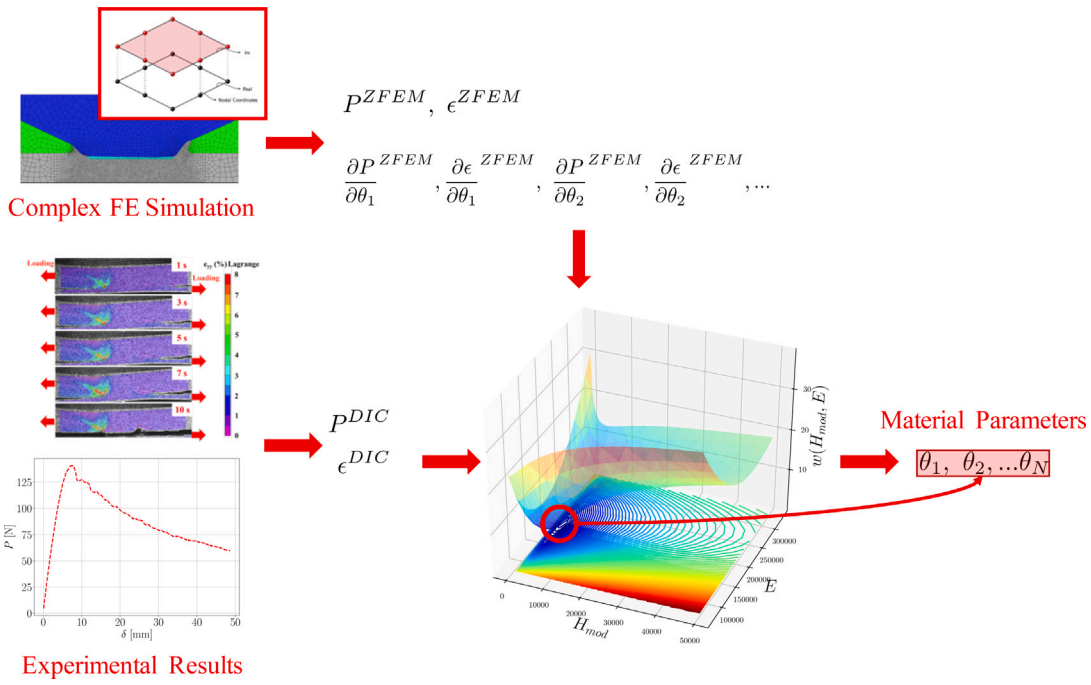

Fig. 10. Optimization flowchart.

Fig. 11. Tensile test sample with speckle pattern (post-fracture).

For each material property in θ, a ZFEM analysis is required to compute the derivative of the residual function (Eq. (12)). Hence, a total of N_θ ZFEM analyses are required per iteration of the nonlinear optimizer.

Fig. 10 shows a schematic of the optimization procedure. A ZFEM analysis provides the traditional FE outputs and their derivatives, such as reaction force and strain fields, with respect to the unknown material properties, as in Eqs. (12) and (13). Then, ZFEM's reaction force and strain field are compared against those obtained using DIC, and a residual function is computed. In addition, derivatives of the residual function with respect to the unknown parameters are computed using ZFEM's derivatives. The derivatives are used to compute a directional derivative that is used to locate a global minimum. The procedure is repeated until a tolerance criterion is satisfied; e.g., the norm of the Jacobian vector is within the desired tolerance, $\|\mathbf{J}(\boldsymbol{\theta})\| \leq tol$.

3. Numerical results

Use of ZFEM gradients within an optimization process to inversely determine material constitutive parameters is demonstrated for two examples. First, the mechanical properties of DP-590 steel were obtained using a tensile test specimen. Second, the cohesive material properties of an adhesively bonded joint were obtained using the proposed approach that combines ZFEM and DIC data.

3.1. Elastic–plastic behavior from a tensile test

A uniaxial tensile test was used to verify the capabilities of the inverse DIC-ZFEM framework by obtaining the yield strength and nonlinear exponent of the Ramberg–Osgood material model (σ_y and n) of DP-590 steel. The elastic properties were assumed to be given and only σ_y and n were treated as unknowns. In this test, a sample was subjected to tension until failure (see Fig. 11).

Table 2
Tensile test sample dimensions.

Dimension	Symbol	Value [mm]
Gauge length	G	25.0 ± 0.1
Width	W	6.0 ± 0.1
Radius of fillet	R	6
Overall length	L	100
Length of the reduced section	A	32
Length of the grip section	B	30
Width of grip section	C	10

This problem was simulated with ZFEM using a Ramberg–Osgood (deformation theory) material model (see Section 2.3.2). The elastic material properties used DP-590 steel were an elastic modulus of E = 200 GPa and a Poisson's ratio of $\nu = 0.3$ (Vedantam et al., 2006). Plane strain conditions were assumed.

The parameters obtained from the optimization procedure were the yield strength, σ_y, and the nonlinear exponent, n. Hence, the solution vector to be obtained from the optimization algorithm was

$$\boldsymbol{\theta} = \begin{bmatrix} \sigma_y \\ n \end{bmatrix} \tag{14}$$

Fig. 12 and Table 2 show the dimensions used for the experiment and the FE simulation. The red shaded region in Fig. 12 denotes the ROI for which the DIC strains were obtained to compute the strain residual, $\boldsymbol{R}_{\epsilon_{yy}}$.

The dog-bone specimen was modeled in 2-D with ZFEM using 16-noded (8 real and 8 imaginary) quadratic complex-variable quadrilateral plane strain elements. Fig. 13 shows the FE mesh, consisting of

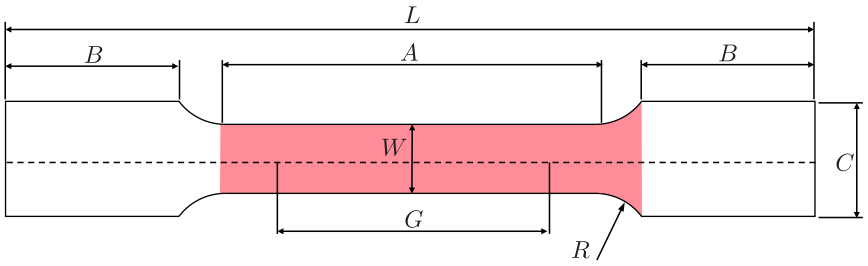

Fig. 12. Tensile test specimen geometry.

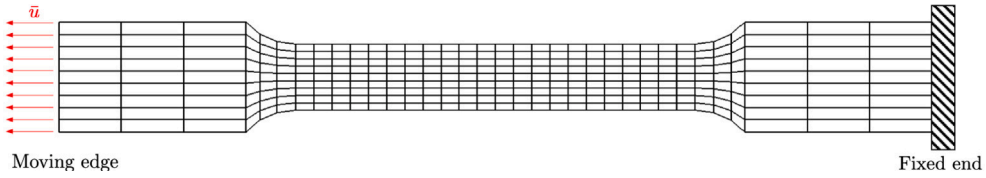

Fig. 13. Finite element model for the tensile test specimen.

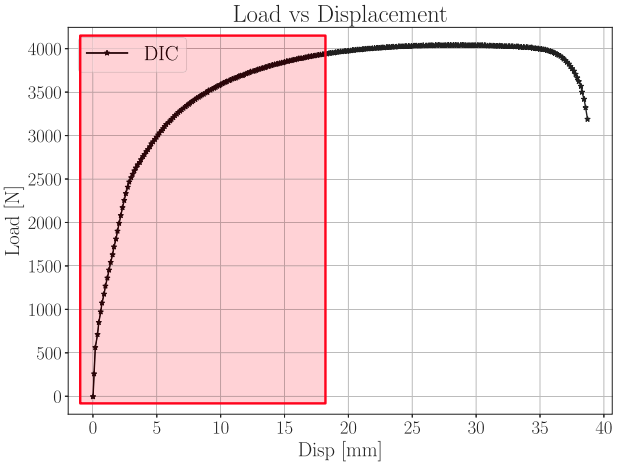

Fig. 14. Force vs. displacement curve for the tensile test.

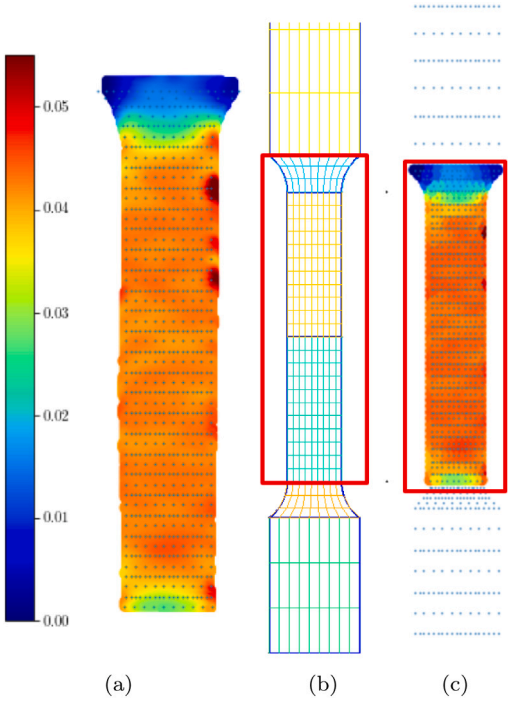

Fig. 15. (a) Strain in the y-direction (ϵ_{yy}) from DIC, (b) FE mesh, and (c) strain field approximated from DIC to the center of the finite elements.

387 elements, and the boundary conditions applied to the model. A displacement was applied to the left edge of the specimen, $\bar{u}$, and the nodes at the right end were fixed in the x- and y-directions.

A DIC image was obtained every 5 s for a total test duration of 1,475 s, resulting in 295 DIC datasets. Fig. 14 shows the Load–Displacement curve corresponding to the test. The red shaded region denotes the increments that were used for the computation of the residual, corresponding to the first 143 increments. This corresponds to all of the loading increments before necking occurs.

The strain fields resulting from the DIC analysis were interpolated to the FE sampling points to compute the residual function to be minimized. For this residual, ϵ_{yy} strains from the center of the finite elements that lie inside the ROI which corresponds to an integration point, were used. Fig. 15(a) shows the DIC strain in the y-direction, ϵ_{yy}, for a particular DIC dataset. Fig. 15(b) shows the FE mesh, in which the red area denotes the elements used in computing the residual and Fig. 15(c) shows the resulting strain fields that were approximated from DIC to the FE mesh.

For this example, the weights of the residuals were chosen as $\alpha_P = 0.5$ and $\alpha_{\epsilon_{yy}} = 0.5$ and a gradient descent method with a fixed step size of 0.1 was used to minimize the residual function. A detailed study on the selection of the residual weights and their effect on the converged results is shown in Section 3.3. An initial educated guess of the parameters to be optimized was

$$\boldsymbol{\theta}_0 = \begin{bmatrix} \sigma_{y_0} \\ n_0 \end{bmatrix} = \begin{bmatrix} 380\,\text{MPa} \\ 8 \end{bmatrix} \tag{15}$$

With ZFEM, no additional function calls were needed to compute the gradient, because the derivatives are a by-product of the complex-variable analysis. For this example involving two parameters, two ZFEM analyses were needed to compute the residual function (Eq. (11)) and its derivative with respect to the variables being optimized for each iteration of the optimizer (Eq. (12)). The convergence criterion for this problem used the norm of the Jacobian vector, i.e., $\left\|\mathbf{J}(\sigma_y, n)\right\| \leq 1\times10^{-4}$.

Fig. 16 shows a three-dimensional representation of the residual function and the iterations that were performed during the minimization process. A close-up of the region where the proposed method

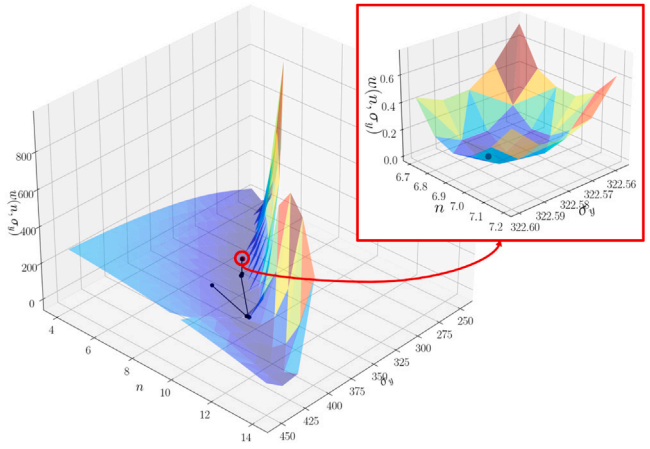

Fig. 16. Three-dimensional representation of the residual function and the steps of the optimization algorithm for the tensile test.

Table 3
Optimization iterations results for tensile test.

Iteration	σ_y [MPa]	n
1	380.00	8.000
2	379.91	9.765
3	379.90	9.884
4	379.64	9.889
5	379.55	9.850
6	341.01	7.665
7	340.63	7.674
8	338.59	7.609
9	323.26	6.881
10	322.58	6.854
11	322.58	6.880
12	322.58	6.884
13	322.58	6.885

converges is also shown. The numerical values of σ_y and n for each iteration are given in Table 3. A total of 26 ZFEM analyses were required.

Fig. 17 shows a comparison of the experimental and computational strain fields. Fig. 17(a) corresponds to the strain field of DIC dataset number 130 out of the 143 that were selected for the minimization process (before necking starts). ZFEM's strain fields corresponding to the initial guess of cohesive parameters are shown in Fig. 17(b) and the converged values are shown in Fig. 17(c). As indicated by the colors of the fields, there is excellent agreement between the experimental and ZFEM converged strain fields.

Fig. 18 compares the stress–strain curves for the converged values of ZFEM against the experimental result. The curve corresponding to the initial guess of Ramberg–Osgood parameters is also plotted for reference. The experimental and optimized ZFEM results (red and blue curves) are in excellent agreement, verifying the accuracy of ZFEM's converged cohesive parameters.

3.2. Adhesively bonded double cantilever beam

A DCB test was used to demonstrate the use of ZFEM's gradients to inversely determine interfacial properties. For this example, the mode-I cohesive parameters determined were the normal fracture energy (ϕ_n), and the maximum normal traction (σ_{max}), see Section 2.2.

Fig. 19 shows the sample (post-fracture) that was used for the DCB test with the white and black speckle pattern required for the DIC analysis. Hinges were glued to the steel sheets with a much stronger adhesive than the one used between the steel sheets.

Fig. 20 illustrates the variables used for the dimensions of the DCB sample: L is the total length of the specimen, L_P is the distance from

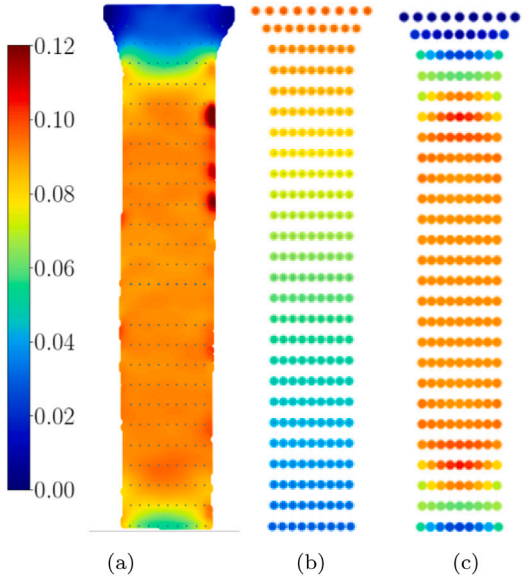

Fig. 17. Strain fields for (a) DIC, (b) initial guess, and (c) converged set of parameters.

Table 4
Dimensions for the DCB test.

Dimension	Symbol	Value [mm]
Length	L	101.6
Initial crack size	a_0	38.57
Distance to applied load	L_P	12.96
Arm height	H	1.016
Specimen width	B	25.4

the free end to the point where the load is being applied, a_0 is the initial crack length, H is the thickness of one sheet, and B is the specimen width.

Using the post-failure adherends, Fig. 21, and the DCB specimen, Fig. 19, the dimensions were retrieved using an image digitizer. The retrieved dimensions are shown in Table 4. As can be observed from Fig. 21, the end of the bond line is offset with respect to the initial or expected location, which was denoted by the marked line. This designated "measured bond line location" was used for reference purposes while selecting the ROI for the DIC test.

The ROI and its location within the sample are shown in Fig. 22 (red shaded area). The blue line corresponds to the marked line in Fig. 21, which denotes the expected bond line (before testing). As can be observed, there is a 2.0 mm offset between the expected and actual bond line locations. The strain values were assigned to the centers of the FEs that lay within the ROI to compute the strain residual during the optimization process; see Section 2.1.3. The gray color in Fig. 22 denotes the DP-590 steel adherends, green denotes the adhesive, and red indicates the ROI.

The DCB was modeled using a total of 5,639 eight-noded ZFEM elements (four real and four imaginary). For the DP-590 steel adherends, linear elastic material behavior was considered as they are not expected to undergo plastic deformation during the test. The known elastic properties were (Vedantam et al., 2006): elastic modulus $E = 209$ GPa and Poisson's ratio $\nu = 0.3$. The FE mesh is shown in Fig. 23. As the DCB test is under pure mode-I loading conditions, the selection of the mode-II parameters does not affect the results. Hence, it can be assumed that $\phi_t = \phi_n$, $\tau_{max} = \sigma_{max}$, $\alpha = \beta$ and $\lambda_t = \lambda_n$. The initial slope indicator in the normal direction was assumed to be $\lambda_n = 0.005$ as this is the same values used in Ramirez-Tamayo et al. (2021), Park and Paulino (2012) in their verification examples. Finally, the shape parameter in the normal direction was assumed to be $\alpha = 2$. When the shape parameters $\alpha \approx 2$

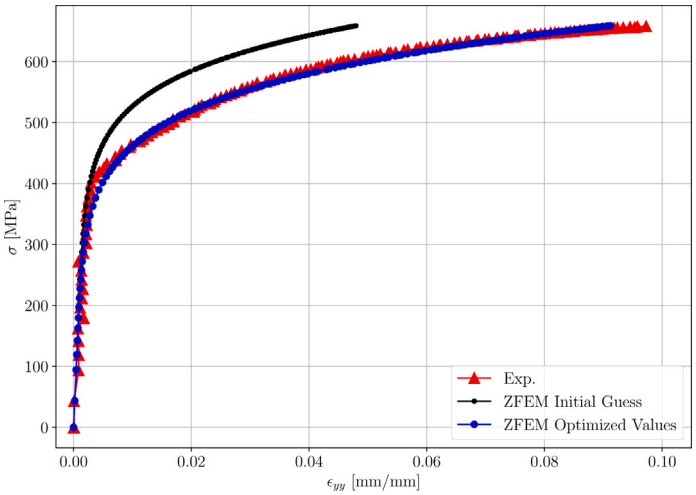

Fig. 18. Stress vs. strain optimization results.

Fig. 19. DCB sample with speckle pattern (post-fracture).

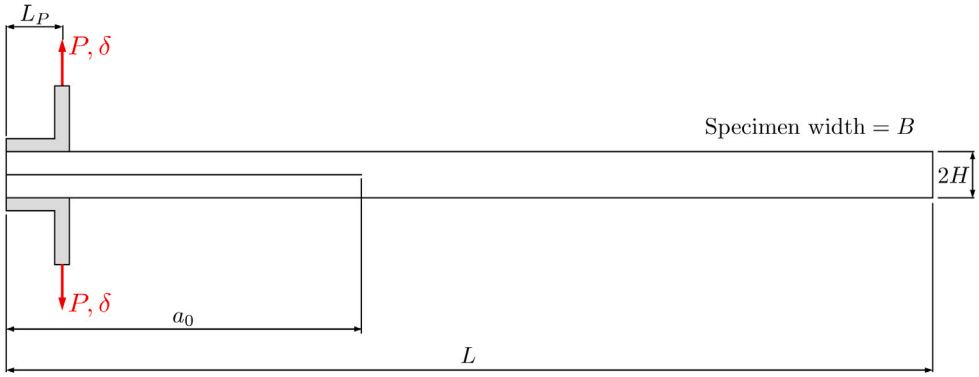

Fig. 20. Schematic of the DCB sample.

and $\beta \approx 2$, the PPR model exhibits an almost linear softening (post-peak load) behavior (Ramirez-Tamayo et al., 2021).

The conjugate gradient method available in SciPy (Virtanen et al., 2020) was used to minimize the residual function with the gradients provided by ZFEM. The convergence criterion for this problem used the norm of the Jacobian vector, i.e., $\|\mathbf{J}(\phi_n, \sigma_{max})\| \leq 1 \times 10^{-4}$. Because two variables are being optimized, two ZFEM analyses were required per iteration of the nonlinear optimizer to compute the gradient vector. The weights of the load and strain residuals were $\alpha_P = 0.5$ and $\alpha_{\epsilon_{yy}} = 0.5$, respectively. An initial educated guess (Ramirez-Tamayo et al., 2021) was then provided to the optimizer:

$$\boldsymbol{\theta_0} = \begin{bmatrix} \phi_{n_0} \\ \sigma_{max_0} \end{bmatrix} = \begin{bmatrix} 0.350 \\ 10.0 \end{bmatrix} \tag{16}$$

After 14 iterations of the optimizer, the solution converged to the following values:

$$\boldsymbol{\theta} = \begin{bmatrix} 2.060 \\ 14.07 \end{bmatrix} \tag{17}$$

A comparison of the load–displacement curve obtained with ZFEM's converged values is shown in Fig. 24. The curve corresponding to the initial guess of cohesive parameters is also plotted. The experimental and converged computational curves are in good agreement. The red dot in the experimental curve denotes the last load increment that was used for computing the residuals. After this point, necking was observed in the experimental results.

Fig. 25 shows the strain and load relative difference between experimental and computational results as a function of the loading increment (40 increments in total) for the converged set of cohesive parameters.

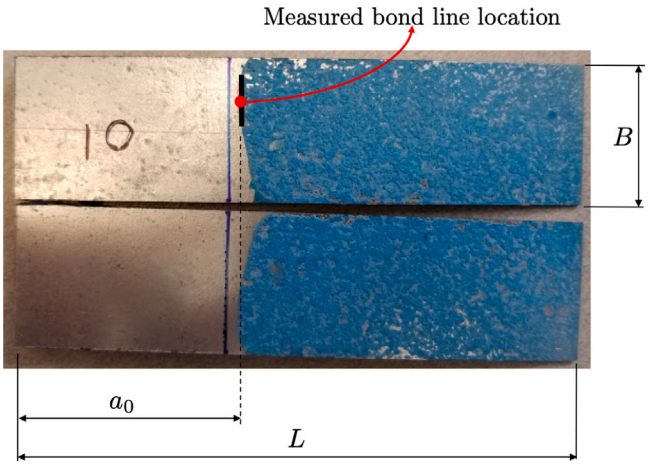

Fig. 21. Adherend surfaces after fracture.

The strain relative difference reported was averaged over all nodes at each loading increment. As it can be observed in Fig. 25(a), the strain error is relatively low before reaching the peak load near the 25th increment. However, once the peak load is reached and softening occurs, the discrepancy between experimental and computational strains increases with a maximum discrepancy of 33.956% in the 39th increment. It is worth mentioning that up to the 30th increment, the relative error is below 1.184%. The critical debonding of the plates that occurs after the 30th increment is likely the reason of the increase in the relative difference of the strains. Fig. 25(b) shows the load relative difference between experimental and computational results as a function of the loading increment with a maximum discrepancy of 2.164% in the 16th increment. The average relative difference between experimental and computational results was 3.92% for the strains and 1.05% for the load. Further improvement could be obtained by adding the PPR variables that govern the softening behavior (λ_n, λ_t, α, and β) in the optimization process. As it currently stands, those parameters were chosen based on those used in Ramirez-Tamayo et al. (2021), Park and Paulino (2012) in their verification examples. An additional source of discrepancy could be the uncertainty arising from the experiment itself, including geometry, test set up, DIC measurements, etc.

3.3. Influence of residual weights on optimized parameters

In this paper, a weighted residual formulation was proposed to incorporate both local and global behavior during the optimization procedure. Recall that the residual function is computed as

$$w(\phi_n, \sigma_{max}) = \alpha_P \left\| \boldsymbol{R}_P \right\|^2 + \alpha_{\epsilon_{yy}} \left\| \boldsymbol{R}_{\epsilon_{yy}} \right\|^2 \tag{18}$$

where the local behavior is added to the residual function through the strain fields and the global behavior through the load–displacement curve. In all the numerical examples discussed in this paper, the residual weights were $\alpha_P = \alpha_{\epsilon_{yy}} = 0.5$, granting the same importance to both the local and global behaviors. In this section, different combinations of residual weights were considered to assess their influence on the optimized set of parameters for the DCB test discussed in Section 3.2. Seven cases were analyzed, including a solely load-based residual ($\alpha_P = 1$, $\alpha_{\epsilon_{yy}} = 0$) and a solely strain-based residual ($\alpha_P = 0$, $\alpha_{\epsilon_{yy}} = 1$). The parameters for each case and the results are summarized in Table 5. For these results, the convergence criterion had to be increased from $\left\| \mathbf{J}(\phi_n, \sigma_{max}) \right\| \leq 1 \times 10^{-4}$ to $\left\| \mathbf{J}(\phi_n, \sigma_{max}) \right\| \leq 5 \times 10^{-2}$, because Cases 1 and 2 did not converge with the previous tolerance that was used in the examples discussed in Sections 3.1 and 3.2. These results used the same initial guess of cohesive parameters as in example 3.2; see Eq. (16).

Table 5
Results for different combination of residual weights.

Case ID	Weights		Residuals			Optimized values	
	α_P	$\alpha_{\epsilon_{yy}}$	$\boldsymbol{R}_P$ [%]	$\boldsymbol{R}_{\epsilon_{yy}}$ [%]	$w(\phi_n, \sigma_{max})$ [%]	ϕ_n	σ_{max}
1	1.0	0.0	2.353	9.382	2.353	1.557	14.018
2	0.9	0.1	1.791	7.726	2.358	1.608	14.041
3	0.7	0.3	1.204	5.447	2.481	1.700	14.033
4	0.5	0.5	1.056	3.221	2.489	1.789	14.004
5	0.3	0.7	1.174	3.026	2.471	1.857	13.999
6	0.1	0.9	1.329	2.626	2.492	1.899	13.986
7	0.0	1.0	1.426	2.427	2.427	1.918	13.993

The residuals shown in Table 5 can be interpreted as the average relative error between the computational and experimental results. Case 1, which did not use the strain fields to compute the residual function, shows a good relative error for the load. However, this is not the case for the strain fields where a higher relative error is obtained. This indicates that the strain fields (local behavior) should be added to the residual formulation. This is confirmed in the following cases, where increasing the weight of the strain residual ($\alpha_{\epsilon_{yy}}$) reduces the relative error of both the reaction-force and strain-field residuals. As can be observed, if $\alpha_{\epsilon_{yy}} > \alpha_P$, the relative error of the strains is repeatedly reduced, but this is not the case for the load relative error where it increases. Hence, an equally weighted residual formulation ($\alpha_P = \alpha_{\epsilon_{yy}} = 0.5$) is recommended to achieve the optimum combination of relative error for both residuals. As can be expected, different weights results in different optimized values. In particular, adding the effect of the strain fields leads to a higher normal fracture energy (ϕ_n). In contrast, the values for the maximum normal traction (σ_{max}), are almost the same regardless of the combination of weights used.

Fig. 26 shows a comparison of the load–displacement curves obtained with the different combinations of weights vs. the experimental results. As can be observed, once $\alpha_{\epsilon_{yy}} \geq 0.3$, the computational and experimental results agree well. When $\alpha_{\epsilon_{yy}} = \alpha_P = 0.5$, excellent agreement is observed, thus verifying the importance of adding DIC data to the optimization procedure through a weighted residual formulation. Compared to the results shown in Fig. 24, where the residual weights were also $\alpha_{\epsilon_{yy}} = \alpha_P = 0.5$, there is a small variation on the converged results. This is due to the fact that the tolerance used in this example was increased because Cases 1 and 2 did not converge with the previous criterion.

4. Discussion

The additional computational cost when using the ZPPR element is 50% more than that for a real-variable PPR element. The increase in runtime is a result of the additional degrees of freedom needed to form a complex element and the use of a CR matrix representation to solve the complex-valued system of equations in Abaqus; see Section 2.3.1. Nonetheless, the overall runtime is still less than for a finite difference approach which requires 2 analyses per derivative. However, the runtime for ZFEM can be reduced by implementing a block forward substitution (BFS) solution scheme, as proposed by Aguirre-Mesa et al. (2021).

The use of complex variables in a PPR element, i.e., “ZPPR”, enables computation of highly accurate derivatives of the nodal displacements and post-processing quantities (strain, stresses, and energy) with respect to any input parameter such as shape, material properties, or loading conditions. This approach can be scaled for the computation of higher-order derivatives as shown in Aguirre-Mesa et al. (2019), Ramirez-Tamayo et al. (2020). However, doing so requires a hypercomplex-variable library (Aguirre-Mesa et al., 2020) to perform hypercomplex operations and the computational times are greatly increased as a result. As shown in Aguirre-Mesa et al. (2021), the

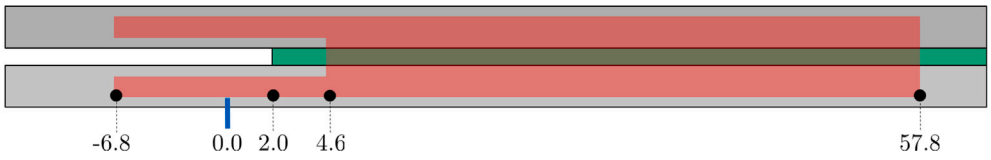

Fig. 22. DIC ROI for the DCB test (dimensions in mm). Figure not to scale.

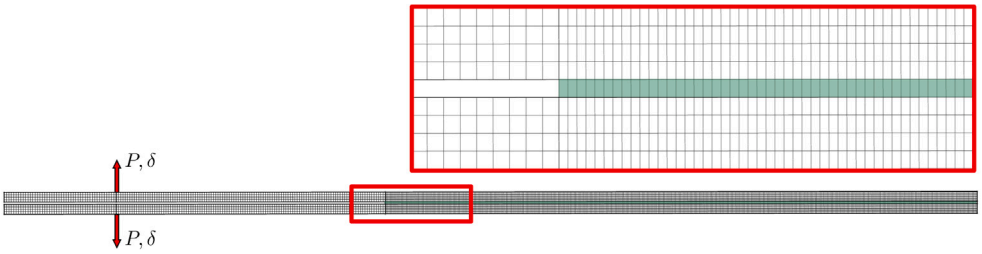

Fig. 23. FE mesh for the DCB specimen.

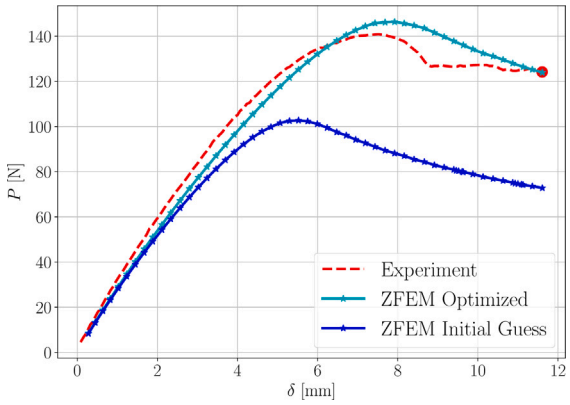

Fig. 24. Comparison of experimental and computational load–displacement curves.

BFS method can be used to solve a hypercomplex system of equations to reduce the additional runtime. This capability could improve ZFEM's convergence during inverse determination of constitutive parameters by providing the Hessian matrix (which requires second-order derivatives) of the objective function to the optimizer.

The proposed methodology can be applied to dissimilar joints produced using, for example, Friction stir Assisted Scribe Technique (FAST) (Wang et al., 2020). By assuming a cohesive behavior at the interface, the cohesive properties that govern the interfacial behavior of the joint can be inversely determined using DIC and load–displacement data. The existing mechanical test techniques to obtain the parameters for a cohesive law place restriction on the test geometries and sometimes require the existence of analytical solutions, making those techniques unsuitable for FaST obtained joints. In addition, the existing techniques use a global response (load–displacement curve) to describe a local material property which results in inaccuracies on the adopted model as shown in Section 3.3.

Section 3.3 showed the effect of incorporating DIC strain data to the minimization process. If a load-based residual ($\alpha_P = 1, \alpha_{\epsilon_{yy}} = 0$) formulation is used, there is a noticeable discrepancy between computational and experimental load–displacement curves during softening; see Fig. 26. The discrepancy was improved by using a weighted residual formulation. However, there is still some discrepancy for this case. Further improvement could be obtained by adding the PPR variables that govern the softening behavior (λ_n, λ_t, α, and β) in the optimization process. As it currently stands, those parameters were chosen based on those used in Ramirez-Tamayo et al. (2021), Park and Paulino (2012) in their verification examples. An additional source of discrepancy could be the uncertainty arising from the experiment itself, including geometry, test set up, DIC measurements, etc.

5. Conclusions

This paper demonstrated the use of a complex-variable finite element method-based inverse methodology to extract constitutive parameters using experimental data. A weighted residual optimization method that combined full-field kinematic measurements obtained using the digital image correlation (DIC) procedure and load–displacement data was used to determine the optimum constitutive properties. Two examples were demonstrated: (1) determining the Ramberg–Osgood parameters for a DP-590 steel specimen, and (2) determining the interfacial constitutive parameters of an adhesive using a DCB specimen. The results showed that the most accurate parameter values can be determined using a combination of equally-weighted strain fields and load–displacement data, rather than using solely load–displacement data. Minimizing the relative error in both the strain fields and the load–displacement curve is important to obtain accurate interfacial properties.

The use of the complex-variable finite element method, ZFEM, provided efficient and accurate derivatives of kinematic and load–displacement data with respect to the constitutive parameters. These derivatives were critical in minimizing the relative error in an efficient manner. An attractive feature of ZFEM is that it is significantly superior to the finite difference method as the derivative results are largely step-size independent and that it is computationally more efficient. Although the method was demonstrated for two materials, the methodology is general and can be applied to other geometries, materials, and interfaces obtained by a variety of joining methods.

Declaration of competing interest

The authors declare that they have no known competing financial interests or personal relationships that could have appeared to influence the work reported in this paper.

Acknowledgments

PNNL is operated by Battelle for the U.S. Department of Energy under contract DE-AC05-76RL01830. This work was sponsored by the DOE- EERE, Vehicle Technology Office, through the Joining Core Program.

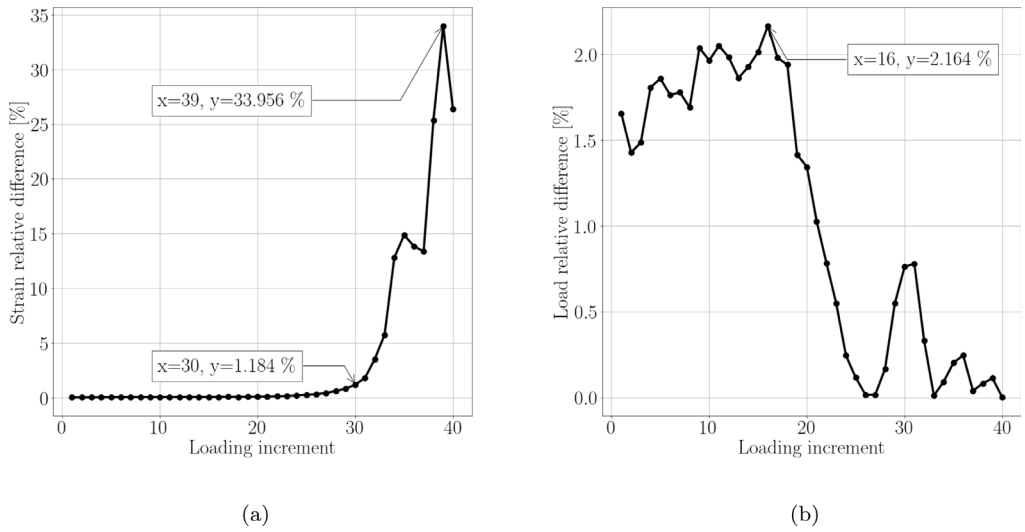

Fig. 25. Relative error vs loading increment for (a) strain and (b) load.

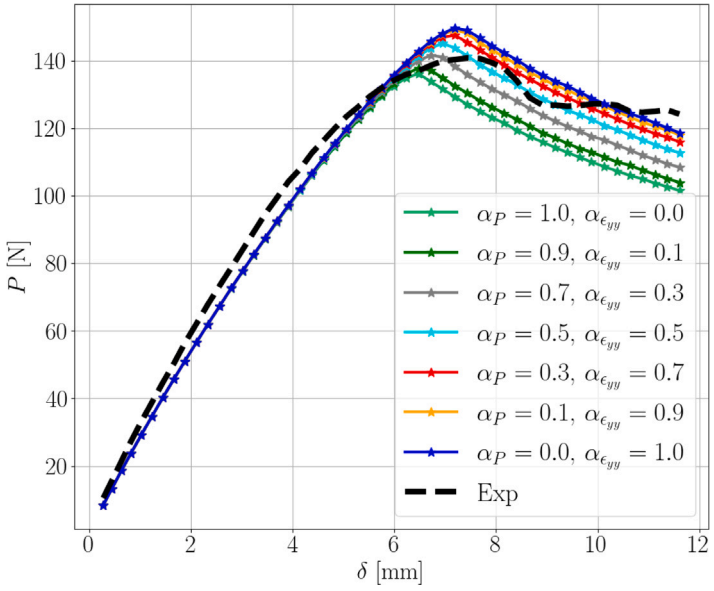

Fig. 26. Load–displacement curve comparison for different combinations of residual weights.

Appendix

Consider the multivariate function $f(x, y, z) = x^3 y^2 z$. To compute a first-order derivative with respect to x, a small perturbation h must be applied along the imaginary axis as $x^* = x + ih$

$$f(x + ih, y, z) = (x + ih)^3 y^2 z \tag{19}$$

$$f(x + ih, y, z) = \left[x^3 + 3x^2(ih) - 3x(ih)^2 + (ih)^3\right] y^2 z \tag{20}$$

Recall from complex-variable algebra that $i^2 = -1$ and $i^3 = -i$:

$$f(x + ih, y, z) = \left[x^3 + 3x^2(ih) - 3xh^2 - ih^3\right] y^2 z \tag{21}$$

Neglecting high order terms, the function yields

$$f(x + ih, y, z) = \left[x^3 + 3x^2(ih) - \cancelto{0}{3xh^2} - \cancelto{0}{ih^3}\right] y^2 z \tag{22}$$

This can be divided into real and imaginary parts:

$$f = \underbrace{x^3 y^2 z}_{\text{Re}} + \underbrace{\left[3x^2\, ih\right] y^2 z}_{\text{Im}} \tag{23}$$

where the real part corresponds to the original function and the imaginary part contains the derivative, as shown in Eq. (3). Then, the derivative of the function with respect to the variable of interest, x, is obtained as follows:

$$\frac{\partial f(x, y, z)}{\partial x} = \frac{\text{Im}[f]}{h} = \frac{3x^2 y^2 z\, h}{h} = 3x^2 y^2 z \tag{24}$$

References

Abaqus, 2015. Abaqus finite element software. Dassault Systèmes Simulia Corp., Providence, RI, 2015.

Aguirre-Mesa, A.M., Garcia, M.J., Aristizabal, M., Wagner, D., Ramirez-Tamayo, D., Montoya, A., Millwater, H., 2021. A block forward substitution method for solving the hypercomplex finite element system of equations. Comput. Methods Appl. Mech. Engrg. 387, 114195. http://dx.doi.org/10.1016/j.cma.2021.114195, https://www.sciencedirect.com/science/article/pii/S0045782521005260.

Aguirre-Mesa, A.M., Garcia, M.J., Millwater, H., 2020. MultiZ: A library for computation of high-order derivatives using multicomplex or multidual numbers. ACM Trans. Math. Software 46 (3), http://dx.doi.org/10.1145/3378538.

Aguirre-Mesa, A.M., Ramirez-Tamayo, D., Garcia, M.J., Montoya, A., Millwater, H., 2019. A stiffness derivative local hypercomplex-variable finite element method for computing the energy release rate. Eng. Fract. Mech. 218, 106581. http:

//dx.doi.org/10.1016/j.engfracmech.2019.106581, URL http://www.sciencedirect.com/science/article/pii/S0013794419306666.
ASTM International, 2001. E8/E8M-01, Standard test methods for tension testing of metallic materials, West Conshohocken, PA.
Barenblatt, G.I., 1959. The formation of equilibrium cracks during brittle fracture. General ideas and hypotheses. Axially-symmetric cracks. J. Appl. Math. Mech. 23 (3), 622–636. http://dx.doi.org/10.1016/0021-8928(59)90157-1.
Correlated Solutions, Inc., 2010. Vic-3D Manual, Columbia, SC.
da Silva, L.F., das Neves, P.J., Adams, R., Spelt, J., 2009. Analytical models of adhesively bonded joints-Part I: Literature survey. Int. J. Adhes. Adhes. 29 (3), 319–330. http://dx.doi.org/10.1016/j.ijadhadh.2008.06.005, URL https://www.sciencedirect.com/science/article/pii/S0143749608000730.
Dugdale, D.S., 1960. Yielding of steel sheets containing slits. J. Mech. Phys. Solids 8 (2), 100–104. http://dx.doi.org/10.1016/0022-5096(60)90013-2.
Ebnesajjad, S., Landrock, A.H., 2014. Adhesives Technology Handbook. William Andrew, Elsevier, URL https://www.elsevier.com/books/adhesives-technology-handbook/ebnesajjad/978-0-323-35595-7.
Freed, Y., Banks-Sills, L., 2008. A new cohesive zone model for mixed mode interface fracture in bimaterials. Eng. Fract. Mech. 75 (15), 4583–4593.
Goland, M., Reissner, E., 2021. The stresses in cemented joints. J. Appl. Mech. 11 (1), A17–A27. http://dx.doi.org/10.1115/1.4009336, arXiv:https://asmedigitalcollection.asme.org/appliedmechanics/article-pdf/11/1/A17/6657406/a17_1.pdf.
Gomez-Farias, A., Montoya, A., Millwater, H., 2015. Complex finite element sensitivity method for creep analysis. Int. J. Press. Vessels Pip. 132–133, 27–42. http://dx.doi.org/10.1016/j.ijpvp.2015.05.006, URL http://www.sciencedirect.com/science/article/pii/S0308016115000587.
Ji, G., Ouyang, Z., Li, G., 2012. Local interface shear fracture of bonded steel joints with various bondline thicknesses. Exp. Mech. 52 (5), 481–491.
Lantoine, G., Russell, R.P., Dargent, T., 2012. Using multicomplex variables for automatic computation of high-order derivatives. ACM Trans. Math. Software 38 (3), 16:1–16:21. http://dx.doi.org/10.1145/2168773.2168774, URL http://doi.acm.org/10.1145/2168773.2168774.
Liljedahl, C., Crocombe, A., Wahab, M., Ashcroft, I., 2006. Damage modelling of adhesively bonded joints. Int. J. Fract. 141 (1), 147–161.
Marzi, S., Biel, A., Stigh, U., 2011. On experimental methods to investigate the effect of layer thickness on the fracture behavior of adhesively bonded joints. Int. J. Adhes. Adhes. 31 (8), 840–850. http://dx.doi.org/10.1016/j.ijadhadh.2011.08.004, URL https://www.sciencedirect.com/science/article/pii/S0143749611001229.
Mi, Y., Crisfield, M., Davies, G., Hellweg, H., 1998. Progressive delamination using interface elements. J. Compos. Mater. 32 (14), 1246–1272. http://dx.doi.org/10.1177/002199839803201401.
van Mier, J.G.M., van Vliet, M.R.A., 2002. Uniaxial tension test for the determination of fracture parameters of concrete: state of the art. Eng. Fract. Mech. 69 (2), 235–247. http://dx.doi.org/10.1016/S0013-7944(01)00087-X, URL http://www.sciencedirect.com/science/article/pii/S001379440100087X.
Millwater, H., Wagner, D., Baines, A., Montoya, A., 2016. A virtual crack extension method to compute energy release rates using a complex variable finite element method. Eng. Fract. Mech. 162, 95–111. http://dx.doi.org/10.1016/j.engfracmech.2016.04.002, URL http://www.sciencedirect.com/science/article/pii/S0013794416301540.
Montoya, A., Fielder, R., Gomez-Farias, A., Millwater, H., 2015. Finite-element sensitivity for plasticity using complex variable methods. J. Eng. Mech. 141 (2), 04014118. http://dx.doi.org/10.1061/(ASCE)EM.1943-7889.0000837.
Montoya, A., Ramirez-Tamayo, D., Millwater, H., Kirby, M., 2018. A complex-variable virtual crack extension finite element method for elastic-plastic fracture mechanics. Eng. Fract. Mech. 202, 242–258. http://dx.doi.org/10.1016/j.engfracmech.2018.09.023, URL http://www.sciencedirect.com/science/article/pii/S0013794418306775.
Pan, B., Li, K., 2011. A fast digital image correlation method for deformation measurement. Opt. Lasers Eng. 49 (7), 841–847. http://dx.doi.org/10.1016/j.optlaseng.2011.02.023, URL https://www.sciencedirect.com/science/article/pii/S0143816611000728.
Park, K., 2009. Potential-Based Fracture Mechanics using Cohesive Zone and Virtual Internal Bond Modeling. University of Illinois at Urbana-Champaign, URL https://www.semanticscholar.org/paper/Potential-based-fracture-mechanics-using-cohesive-Park/2265b61f1080589b6b46d2f84714182d017eaa27.
Park, K., Choi, H., Paulino, G.H., 2016. Assessment of cohesive traction-separation relationships in abaqus: A comparative study. Mech. Res. Commun. 78, 71–78. http://dx.doi.org/10.1016/j.mechrescom.2016.09.004, Recent Advances in Multiscale, Multifunctional and Functionally Graded Materials, URL http://www.sciencedirect.com/science/article/pii/S0093641316301628.
Park, K., Paulino, G.H., 2012. Computational implementation of the PPR potential-based cohesive model in Abaqus: educational perspective. Eng. Fract. Mech. 93, 239–262. http://dx.doi.org/10.1016/j.engfracmech.2012.02.007.
Park, K., Paulino, G.H., 2013. Cohesive zone models: a critical review of traction-separation relationships across fracture surfaces. Appl. Mech. Rev. 64 (6), http://dx.doi.org/10.1115/1.4023110, 060802, arXiv:https://asmedigitalcollection.asme.org/appliedmechanicsreviews/article-pdf/64/6/060802/6073587/amr_64_6_060802.pdf.
Park, K., Paulino, G.H., Roesler, J.R., 2009. A unified potential-based cohesive model of mixed-mode fracture. J. Mech. Phys. Solids 57 (6), 891–908. http://dx.doi.org/10.1016/j.jmps.2008.10.003, URL http://www.sciencedirect.com/science/article/pii/S0022509608001713.
Prasad, S., Carlsson, L.A., 1994. Debonding and crack kinking in foam core sandwich beams-II. experimental investigation. Eng. Fract. Mech. 47 (6), 825–841. http://dx.doi.org/10.1016/0013-7944(94)90062-0.
Quan, D., Murphy, N., Cardiff, P., Ivankovic, A., 2018. The intrinsic fracture property of a rubber-modified epoxy adhesive: Geometrical transferability. Eng. Fract. Mech. 203, 240–249. http://dx.doi.org/10.1016/j.engfracmech.2018.04.035, 8th ESIS TC4 International Conference- Fracture of Polymers, Composites and Adhesives, URL https://www.sciencedirect.com/science/article/pii/S0013794417313309.
Ramalho, L., Campilho, R., Belinha, J., Da Silva, L., 2020. Static strength prediction of adhesive joints: A review. Int. J. Adhes. Adhes. 96, 102451. http://dx.doi.org/10.1016/j.ijadhadh.2019.102451.
Ramberg, W., Osgood, W.R., 1943. Description of Stress-Strain Curves by Three Parameters. Tech. Rep. NACA-TN-902, National Advisory Committee for Aeronautics, URL https://ntrs.nasa.gov/citations/19930081614.
Ramirez-Tamayo, D., Balcer, M., Montoya, A., Millwater, H., 2020. Mixed-mode stress intensity factors computation in functionally graded materials using a hypercomplex-variable finite element formulation. Int. J. Fract. 226 (2), 219–232. http://dx.doi.org/10.1007/s10704-020-00489-5.
Ramirez Tamayo, D., Montoya, A., Millwater, H., 2018. Complex-variable finite-element method for mixed mode fracture and interface cracks. AIAA J. 56 (11), 4632–4637. http://dx.doi.org/10.2514/1.J057231.
Ramirez-Tamayo, D., Montoya, A., Millwater, H., 2018. A virtual crack extension method for thermoelastic fracture using a complex-variable finite element method. Eng. Fract. Mech. 192, 328–342. http://dx.doi.org/10.1016/j.engfracmech.2017.12.013, URL http://www.sciencedirect.com/science/article/pii/S0013794417309049.
Ramirez-Tamayo, D., Soulami, A., Gupta, V., Restrepo, D., Montoya, A., Millwater, H., 2021. A complex-variable cohesive finite element subroutine to enable efficient determination of interfacial cohesive material parameters. Eng. Fract. Mech. 247, 107638. http://dx.doi.org/10.1016/j.engfracmech.2021.107638.
Reeder, J.R., Crews, Jr., J.H., 1990. Mixed-mode bending method for delamination testing. AIAA J. 28 (7), 1270–1276. http://dx.doi.org/10.2514/3.25204.
Shah, S.P., Swartz, S.E., Ouyang, C., 1995. Fracture Mechanics of Concrete: Applications of Fracture Mechanics To Concrete, Rock and Other Quasi-Brittle Materials. John Wiley & Sons, URL https://www.wiley.com/en-us/Fracture+Mechanics+of+Concrete%3A+Applications+of+Fracture+Mechanics+to+Concrete%2C+Rock+and+Other+Quasi+Brittle+Materials-p-9780471303114.
Shen, B., Paulino, G., 2011. Direct extraction of cohesive fracture properties from digital image correlation: a hybrid inverse technique. Exp. Mech. 51 (2), 143–163. http://dx.doi.org/10.1007/s11340-010-9342-6.
Squire, W., Trapp, G., 1998. Using complex variables to estimate derivatives of real functions. SIAM Rev. 40 (1), 110–112. http://dx.doi.org/10.1137/S003614459631241X.
Valoroso, N., Sessa, S., Lepore, M., Cricrì, G., 2013. Identification of mode-I cohesive parameters for bonded interfaces based on DCB test. Eng. Fract. Mech. 104, 56–79. http://dx.doi.org/10.1016/j.engfracmech.2013.02.008, URL http://www.sciencedirect.com/science/article/pii/S0013794413000507.
Vedantam, K., Bajaj, D., Brar, N., Hill, S., 2006. Johnson-cook strength models for mild and DP 590 steels. In: AIP Conference Proceedings, Vol. 845, no. 1. American Institute of Physics, Washington, pp. 775–778. http://dx.doi.org/10.1063/1.2263437.
Virtanen, P., Gommers, R., Oliphant, T.E., Haberland, M., Reddy, T., Cournapeau, D., Burovski, E., Peterson, P., Weckesser, W., Bright, J., et al., 2020. SciPy 1.0: fundamental algorithms for scientific computing in python. Nature Methods 17 (3), 261–272. http://dx.doi.org/10.1016/j.optlaseng.2011.02.023, URL https://www.nature.com/articles/s41592-019-0686-2.
Volkersen, O., 1938. Die nietkraftverteilung in zugbeanspruchten nietverbindungen mit konstanten laschenquerschnitten. Luftfahrtfor Schung 15, 41–47.
Wang, W.-X., Nakata, M., Takao, Y., Matsubara, T., 2009. Experimental investigation on test methods for mode II interlaminar fracture testing of carbon fiber reinforced composites. Composites A 40 (9), 1447–1455.
Wang, T., Ramirez-Tamayo, D., Jiang, X., Kitsopoulos, P., Kuang, W., Gupta, V., Barker, E., Upadhyay, P., 2020. Effect of interfacial characteristics on magnesium to steel joint obtained using FAST. Mater. Des. 192, 108697. http://dx.doi.org/10.1016/j.matdes.2020.108697, URL http://www.sciencedirect.com/science/article/pii/S0264127520302318.
Whitney, J., Browning, C., Hoogsteden, W., 1982. A double cantilever beam test for characterizing mode I delamination of composite materials. J. Reinf. Plast. Compos. 1 (4), 297–313. http://dx.doi.org/10.1177/073168448200100402.
Wittmann, F., Rokugo, K., Brühwiler, E., Mihashi, H., Simonin, P., 1988. Fracture energy and strain softening of concrete as determined by means of compact tension specimens. Mater. Struct. 21 (1), 21–32, URL https://link.springer.com/article/10.1007/BF02472525.
Xu, C., Siegmund, T., Ramani, K., 2003. Rate-dependent crack growth in adhesives: I. Modeling approach. Int. J. Adhes. Adhes. 23 (1), 9–13. http://dx.doi.org/10.1016/S0143-7496(02)00062-3.